
Universiteit
Leiden
The Netherlands

Random-matrix theory and stroboscopic models of topological insulators and superconductors

Dahlhaus, J.P.

Citation
Dahlhaus, J. P. (2012, November 21). *Random-matrix theory and stroboscopic models of topological insulators and superconductors*. *Casimir PhD Series*. Retrieved from https://hdl.handle.net/1887/20139

Version:	Not Applicable (or Unknown)
License:	Leiden University Non-exclusive license
Downloaded from:	https://hdl.handle.net/1887/20139

Note: To cite this publication please use the final published version (if applicable).

Cover Page

Universiteit Leiden

The handle http://hdl.handle.net/1887/20139 holds various files of this Leiden University dissertation.

Author: Dahlhaus, Jan Patrick

Title: Random-matrix theory and stroboscopic models of topological insulators and superconductors

Date: 2012-11-21

Chapter 1

Introduction

1.1 Preface

Considering what we know about Nature, it is quite fascinating how well it can be described by complex mathematical concepts. Among the most impressive examples might well be General Relativity and Quantum Mechanics. In the former the ideas of differential geometry form the heart of what we call curved space-time, while in the latter the world is described by states and operators in a Hilbert space.

Another intriguing area of mathematics - topology - is by now understood to govern the nature of gapped electronic systems like band insulators or superconductors [1–5]. And it has profound impact on their properties. Most importantly, the boundary between electronic systems with different topology supports protected surface states – robust against disorder and other imperfections. From Majorana bound states at the ends of superconducting wires to the unique metallic surface of three dimensional topological insulators a variety of different boundary states arise in this way – depending on the dimensionality and the symmetries of the system.

The consequences of band topology have by now been observed in several systems, foremost in the form of the quantum Hall and quantum spin Hall effects in two dimensions and the topological insulator in three dimensions. Furthermore, the first signatures of topological superconductivity have been found in nanowire setups.

The primary methods of identification of these phases are their unique transport properties: in the quantum Hall effect, perfectly transmitting

edge channels lead to a quantized Hall conductance, the quantum spin Hall effect shows quantized two- and four-terminal conductances and Majorana bound states show up as a zero bias peak in the Andreev conductance. Only three-dimensional topological insulators are, up to now, identified by spectroscopy rather than by electronic transport, because of the complication of a non-zero bulk conductance.

This work is dedicated to the interplay of topology and imperfections in insulators and superconductors. On the one hand a realistic understanding of the transport signatures of topological phases in the presence of disorder is vital to explain experimental data. On the other hand the interplay of topology and imperfections leads to interesting new phenomena such as delocalization at topological phase transitions and geodesic scattering. We study the thermal and Andreev conductances of chaotic superconducting quantum dots, the effect of disorder on the electrical conductance of normal-superconductor junctions, and the influence of surface roughness on the conductance of a topological insulator. Furthermore we investigate the localization properties at a topological phase transition, estimating the universal critical exponent that describes the observed delocalization for both the quantum Hall and the quantum spin Hall effect.

1.2 Concept of topology in insulating systems

What is a topological phase? I will try to give an intuitive approach to the topic, using examples and concentrating on topics that will be of interest later on in this thesis. From the band theory of solids we know that the electronic excitations of condensed matter systems appear in the form of energy bands $E(\boldsymbol{k})$ with corresponding Bloch states $\psi(\boldsymbol{k})$, $\boldsymbol{k}$ being a wave vector in the first Brillouin zone. In an insulating system, the Fermi energy lies in an excitation gap between such bands. Now, a topological property is by definition something that is preserved under continuous deformations, in this case of the Hamiltonian. A simple example is most suitable to illustrate how this concept applies to band structures.

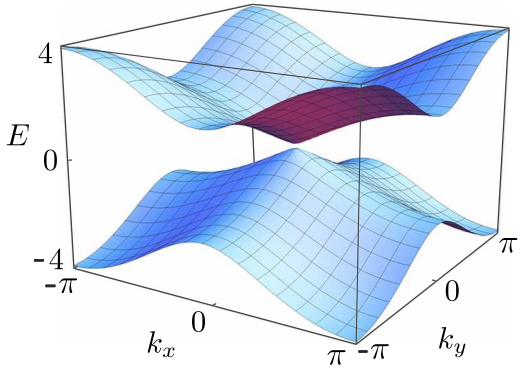

Figure 1.1. Band structure for $\mu = 1.9$. At the center of the Brillouin zone a Dirac cone emerges, which will be fully formed when the gap closes at $\mu = 2$.

1.2.1 Example: winding number

Consider the Hamiltonian

$$H(\boldsymbol{k}) = \boldsymbol{u}(\boldsymbol{k}) \cdot \boldsymbol{\sigma} = \begin{pmatrix} \sin k_x \\ \sin k_y \\ \cos k_x + \cos k_y - \mu \end{pmatrix} \cdot \begin{pmatrix} \sigma_x \\ \sigma_y \\ \sigma_z \end{pmatrix}, \tag{1.1}$$

with the Pauli matrices σ_i and momenta $k_x, k_y \in [-\pi, \pi)$ in the first Brillouin zone of a two-dimensional system. The two bands of the model, $E_\pm(\boldsymbol{k}) = \pm|\boldsymbol{u}(\boldsymbol{k})|$, are plotted in Fig. 1.1 for $\mu = 1.9$.

In this example, the notion of topology manifests itself in the spin structure of the wave functions. The spin quantization axis for given $\boldsymbol{k}$ is $\hat{\boldsymbol{u}}(\boldsymbol{k}) = \boldsymbol{u}(\boldsymbol{k})/|\boldsymbol{u}(\boldsymbol{k})|$. In Fig. 1.2 this vector is plotted in the Brillouin zone for two different values of μ. For $\mu = 1$, the vector shows a winding while for $\mu = 3$ it does not. With "winding" we mean the number of complete rotations the vector performs throughout the Brillouin zone. Due to the periodicity of the Brillouin zone it is an integer quantity and can be calculated by

$$\mathcal{I} = -\frac{1}{4\pi} \int_{-\pi}^{\pi} dk_x \int_{-\pi}^{\pi} dk_y \left[\frac{\partial \hat{\boldsymbol{u}}(\boldsymbol{k})}{\partial k_x} \times \frac{\partial \hat{\boldsymbol{u}}(\boldsymbol{k})}{\partial k_y} \right] \cdot \hat{\boldsymbol{u}}(\boldsymbol{k}). \tag{1.2}$$

A winding of a vector of this form is preserved under continuous deformations of the Hamiltonian $H(\boldsymbol{k})$ and is thus a topological property. Since the integer number $\mathcal{I}$ characterizes the topology, it is called topological invariant or in this specific case Skyrmion number. The integrand

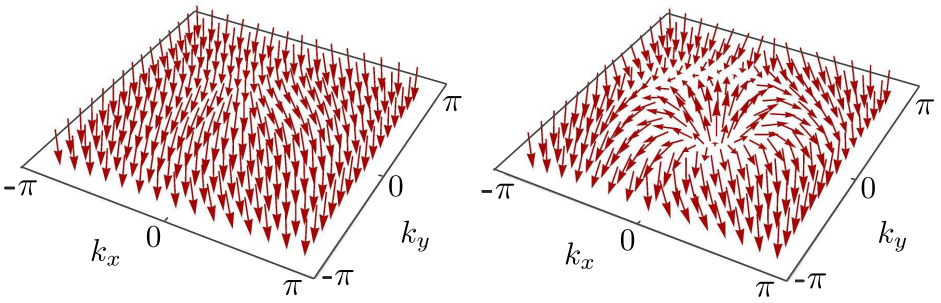

Figure 1.2. Spin quantization axis in the Brillouin zone for a topologically trivial phase, $\mu = 3$ (left panel), and a phase that shows a non-trivial winding, $\mu = 1$ (right panel). The winding can best be seen along the line $k_x = 0$, where the vector makes a complete rotation as it goes from $-\pi$ to π.

of Eq. (1.2) is the so-called Berry flux and the overall integral relates to the Berry phase picked up by a state $\psi(\boldsymbol{k})$ of the lower band when $\boldsymbol{k}$ is transported through the Brillouin zone in a closed loop. In this simple example the topological invariant represents the phase picked up when a spin is rotated once around.

The topological invariant cannot change when we change the Hamiltonian continuously as long as $\boldsymbol{u}(\boldsymbol{k}) \neq (0,0,0)$ for all $\boldsymbol{k}$. Thus the gap between the two bands has to vanish when the topology changes, which happens e.g. for $\mu = 2$ at $(k_x, k_y) = (0,0)$. In overall the model supports the following phases, depending on the value of μ:

$$\mathcal{I}(\mu) = \begin{cases} -\text{sign}\,(\mu) & \text{if } |\mu| < 2, \\ 0 & \text{if } |\mu| > 2. \end{cases} \tag{1.3}$$

The closing of the energy gap is a general feature appearing generically at the transition between two different topological phases.

1.2.2 Boundary states

Maybe the most striking consequence of band topology appears at the boundary of a topological phase. Imagine an interface between a topological region (e.g. $\mathcal{I} = 1$) and a trivial region ($\mathcal{I} = 0$). Interpolation of the Hamiltonian between the two regions requires a change of topology which is accompanied by a closing of the energy gap. Therefore there have to be low-energy electronic states in the region where the energy

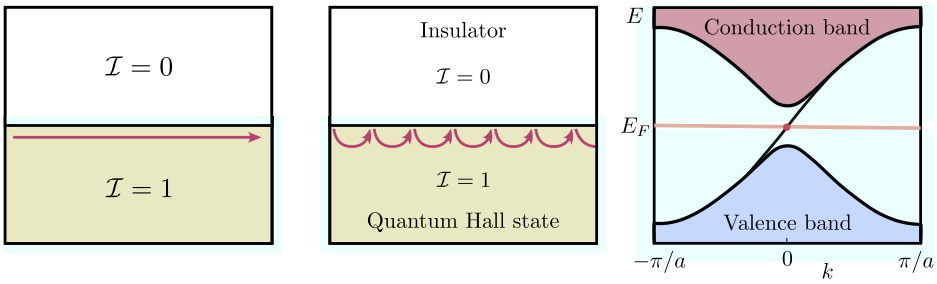

Figure 1.3. Left panel: Topologically protected state propagating along the edge of a region with non-trivial winding number. Middle panel: in the conventional quantum Hall effect, edge states arise in the presence of a strong magnetic field due to the motion electrons perform as their cyclotron orbits bounce repeatedly off the edge of the sample. Right panel: Energy spectrum showing the two bulk bands and the dispersion of the edge state.

gap passes through zero. In other words we find boundary states with energies in the bulk gap.

For the toy model above, these boundary states propagate in one direction along the edge of a sample, see Fig. 1.3. Since there are no states into which they could backscatter, they are insensitive to disorder. A change of sign of the topological invariant reverses the direction of propagation.

The edge states are a feature that our model has in common with the quantum Hall effect, rooted in exactly the same concept of topology. For the quantum Hall effect, there is an intuitive understanding for the existence of edge states: they arise due to the motion electrons perform in a strong magnetic field as their cyclotron orbits bounce repeatedly off the edge of the sample. The presence of the perfectly transmitting edge states leads to a quantized Hall conductance: $G_H = \mathcal{I} G_0$ with the conductance quantum $G_0 = e^2/h$. Unlike the conventional quantum Hall effect the model above (taken from Ref. [6]) does not originate in Landau level quantization – it is called quantum anomalous Hall effect.

1.2.3 Role of symmetries and dimensionality

The example studied so far is in the quantum Hall universality class, which means that it lacks time-reversal symmetry. Indeed symmetries play a crucial role for the existence and the nature of topology in a system [7]. For example the presence of time-reversal symmetry in a

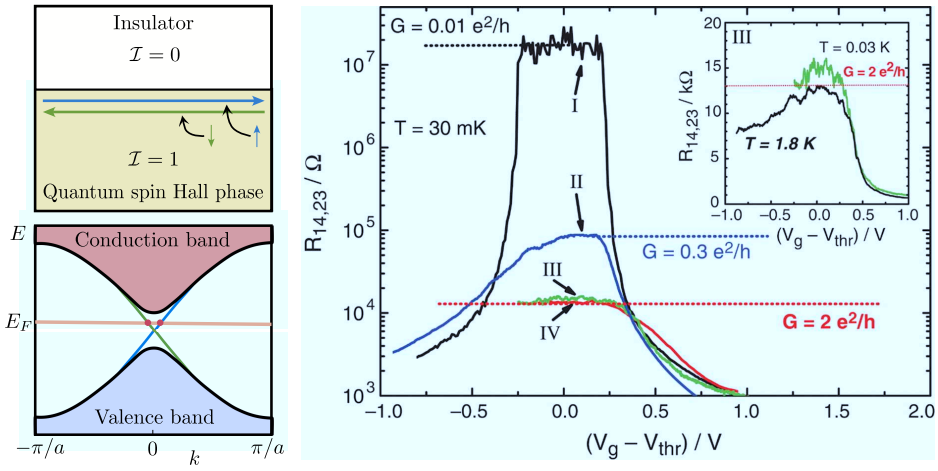

Figure 1.4. Edge states and transport measurements of the quantum spin Hall effect. Upper panel: counter-propagating pair of topologically protected states with opposite spin at the edge of a quantum spin Hall phase. Left lower panel: Energy spectrum showing the two bulk bands and the dispersion of the edge states. Right panel: Experimental data for the conductance of a quantum spin Hall sample, as a function of the gate voltage that tunes the Fermi energy E_F through the bulk gap. Sample I is in the trivial state, showing insulating behavior, while samples III and IV show quantized transport associated with edge states. From Ref. [8]. Reprinted with permission from AAAS.

spinfull system,

$$H(\boldsymbol{k}) = \sigma_y H^*(-\boldsymbol{k})\sigma_y, \tag{1.4}$$

forbids any winding of the type described above in an isolated band. Thus it was long thought that the existence of topology becomes impossible in the presence of time-reversal symmetry. When starting from 2005, theoretical proposals for topology in time-reversal invariant systems were put forward, the research area saw a rapid boost of activity [1–3]. This culminated in the experimental demonstration [8] of the so-called quantum spin Hall effect in 2007, demonstrating that the concept of topology is much more general than and not restricted to the winding numbers introduced above.

The quantum spin Hall effect is a time-reversal invariant version of the quantum Hall effect. Time-reversal symmetry ensures that an edge state always comes hand in hand with its time-reversed partner, a state

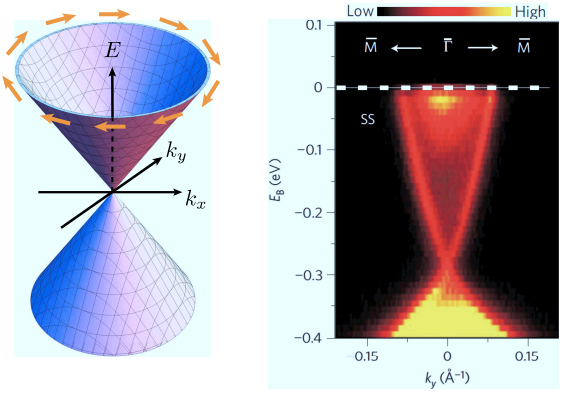

Figure 1.5. Topologically protected states on the surface of a three-dimensional topological insulator. Left panel: Dispersion relation of the metallic surface (Dirac cone). The spin direction is tied perpendicular to the momentum (orange arrows). Right panel: Energy spectrum of the surface states of the topological insulator Bi_2Se_3, measured by angle-resolved photo-emission spectroscopy. From Ref. [10]. Reprinted by permission from Macmillan Publishers Ltd.

with opposite spin, traveling in the reverse direction along the edge (see upper panel of Fig. 1.4).

A fundamental difference between the quantum Hall and the quantum spin Hall effect is that the topological invariant is restricted to the values 0 and 1 in the latter case, meaning either a pair of topologically protected edge states or none at all. The emphasize is here on the topological protection - further edge states may exist but would not be stable. In contrast the quantum Hall effect can realize any integer number of topologically protected edge modes, but they all propagate in the same direction. This ensures the topological protection: if there was a channel in the opposite direction, left and right moving states could scatter into each other and would hybridize, leading to a gap in the spectrum of edge states. In the quantum spin Hall effect this is prevented for a single pair of time reversed modes since the so-called Kramers degeneracy of the crossing point in the Brillouin zone (see lower panel of Fig. 1.4) is protected by time-reversal symmetry.

The two cases mentioned so far are intrinsically two-dimensional. When in 2008 topology was first observed in three dimensions [9], it was a huge step forward on the path to unravel all the possibilities that topology provides. Although conceptually the topology of the three-

dimensional topological insulator is a natural generalization of the quantum spin Hall effect, its properties are exceptional: instead of a pair of edge states, a three-dimensional topological insulator hosts a continuum of surface states, forming a metallic surface of in insulating bulk. Its dispersion has the form of a Dirac cone, see Fig. 1.5, with the spin perpendicular to momentum.

Generally the existence of topology and the allowed values of the topological invariant are determined by the dimensionality of a system and the symmetries present. For insulators, time reversal symmetry plays the primary role in the classification. For superconducting systems which are discussed in the next section, another type of fundamental symmetry arises (particle-hole symmetry) and provides an even larger variety of topological phases.

1.2.4 Anderson localization and topology

The free (ballistic) motion of a particle produces a quadratic spreading of a wave packet in time, $\langle\psi(t)|\hat{x}^2|\psi(t)\rangle \propto t^2$. A disordered potential slows down the spreading, to a linear increase $\langle\psi(t)|\hat{x}^2|\psi(t)\rangle = Dt$. This diffusive spreading, with diffusion constant D, describes a metal. If the disorder is strong enough, the metal becomes an insulator and the spreading stops at a characteristic length ξ,

$$\lim_{t\to\infty}\langle\psi(t)|\hat{x}^2|\psi(t)\rangle \sim \xi^2. \tag{1.5}$$

This so-called Anderson localization [11, 12] originates from destructive interference processes of the wave function and is thus a purely quantum mechanical phenomenon.

Anderson localization happens on shorter length scales in lower dimensional systems. In particular, the localization length grows linearly with the mean free path in one dimension, while it grows exponentially in two dimensions. In three dimensions the localization length is infinite below a critical disorder strength. At the critical disorder strength U_c a quantum phase transition occurs between a localized insulating phase and a diffusive metallic phase. The divergence of the localization length when the disorder strength U approaches U_c is governed by a critical exponent ν,

$$\xi \propto |U - U_c|^{-\nu}. \tag{1.6}$$

The critical exponent is a universal quantity depending only on the fundamental symmetries and the dimensionality, but not on microscopic details.

Anderson localization refers to states in the bulk of a disordered material. States may still be extended along the boundary, without any localization. These extended boundary states are a signature of a topologically nontrivial phase. Figs. 1.3 and 1.4 show examples in the quantum Hall effect and quantum spin Hall effect. The extended boundary states in these two cases carry electrical current along the edge of the system, with a quantized conductance. In a three-dimensional topological insulator, the surface supports extended states, but there is no quantization of conductance in that case.

The appearance and disappearance of extended boundary states is a topological phase transition. Because it is accompanied by a divergence of the localization length in the bulk of the system, it is also associated with a critical exponent, as in Eq. (1.6).

1.3 Topological superconductors

Just like insulators, superconductors have a gapped band structure. In this sense they are insulating as well - but for thermal instead of charge transport. Thus the concept of topology introduced above for insulating systems holds in the same way for superconductors. The presence of another fundamental symmetry (particle-hole symmetry) in a superconductor introduces new features though, as we discuss now.

On mean-field level, superconductors can be described by the Bogoliubov de Gennes Hamiltonian

$$H_{\mathrm{BdG}}(\boldsymbol{k}) = \begin{pmatrix} H_0(\boldsymbol{k}) - E_F & \Delta(\boldsymbol{k}) \\ -\Delta^*(-\boldsymbol{k}) & E_F - H_0^*(-\boldsymbol{k}) \end{pmatrix}, \tag{1.7}$$

with the single particle Hamiltonian $H_0(\boldsymbol{k})$, the Fermi energy E_F and the superconducting pair potential $\Delta(\boldsymbol{k})$. This Hamiltonian acts on two-component wave functions $\psi = (u, v)$ with electron part u and hole part v. With "hole" we mean an empty state in the conduction band, below the Fermi level. This should not be confused with the concept of a hole in a semiconductor, which refers to an empty state in the valence band.

Because electrons and holes in a superconductor refer to the same state, either filled or empty, there is a symmetry relation between elec-

trons and holes,

$$H_{\mathrm{BdG}}(\boldsymbol{k}) = -\tau_x H^*_{\mathrm{BdG}}(-\boldsymbol{k})\tau_x, \tag{1.8}$$

with the Pauli matrix τ_x acting in electron-hole space. The existence of this so-called particle-hole symmetry allows for new topological phases, just like time-reversal symmetry does [7].

Of particular interest are one-dimensional topological superconductors with broken time-reversal and spin-rotation symmetry. They can be realized in semiconductor - superconductor heterostructures (see Fig. 1.6) and their topologically protected end states are Majorana bound states – zero energy eigenstates that are their own electron-hole conjugate partners. These Majorana states are regarded as promising candidates for the realization of a topological quantum memory. In the following section this example is discussed from a transport perspective.

1.3.1 Example: Majorana wire

To illustrate how the concept of topology survives in a disordered system, I will now introduce the scattering approach to topology in a superconducting wire. To this end the wire is contacted by a metallic lead, just as in the experimental situation shown in Fig. 1.6.

When an electron moving inside the lead hits the superconductor, it is reflected back since transmission through the superconductor is suppressed by the superconducting gap. A unitary reflection matrix r relates incoming electronic states ψ_{in} to outgoing electronic states ψ_{out} at the interface (see Fig. 1.6):

$$\psi_{\mathrm{out}} = r\psi_{\mathrm{in}} = \begin{pmatrix} r_{ee} & r_{eh} \\ r_{he} & r_{hh} \end{pmatrix} \psi_{\mathrm{in}}. \tag{1.9}$$

The block r_{he} (r_{eh}) describes the process of Andreev reflection, where an electron (hole) hitting the superconductor is reflected as a hole (electron) while a Cooper pair is added to (removed from) the superconductor. This process is associated with a charge transfer of $2e$, leading to an electrical conductance of

$$G_{\mathrm{NS}} = G_0 \mathrm{Tr}\, r^\dagger_{\mathrm{he}} r_{\mathrm{he}}, \tag{1.10}$$

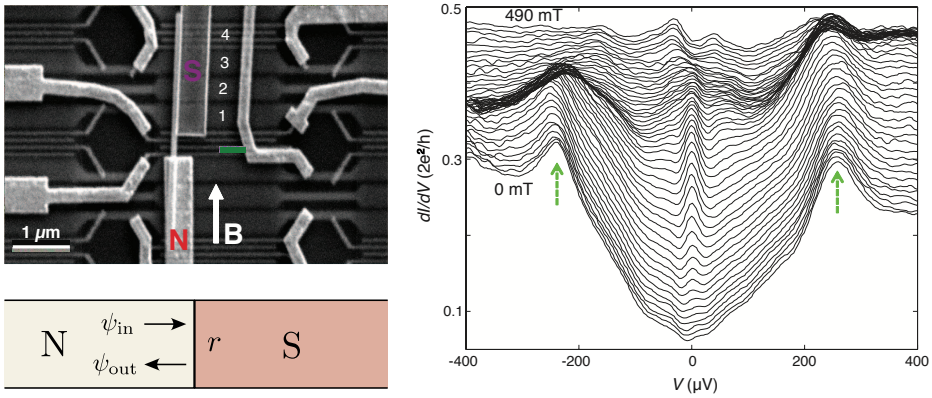

Figure 1.6. Upper panel: Scanning electron microscope image of a device designed to realize a one-dimensional topological superconductor: an InSb nanowire in proximity to a superconductor (S) is contacted by a normal metal lead (N). In the presence of a magnetic field, the wire is expected to make a transition into a topological state. Right panel: Differential conductance measurements for the setup on the left, as a function of bias voltage and magnetic field. For a range of magnetic field strengths a clear zero bias signature is observed in between the two superconducting gap peaks (green arrows), signaling the existence of Majorana bound states. Both from Ref. [13]. Reprinted with permission from AAAS. Lower panel: Schematic of the transport situation.

at zero bias voltage. Here, conductance was measured in units of the superconducting conductance quantum $G_0 = 2e^2/h$.

At the Fermi level (zero excitation energy), particle-hole symmetry requires $r_{hh} = r_{ee}^*$ and $r_{eh} = r_{he}^*$. Therefore the determinant of r has to be real. Since unitarity on the other hand forces the determinant to be of magnitude one, the number

$$Q = \det r \tag{1.11}$$

is a well defined integer, restricted to the two values $+1$ and -1. Because Q cannot change by any small perturbation of the Hamiltonian, it is a topological invariant. To change the value of this number, transmission through the superconductor has to become possible, breaking the unitarity of the reflection matrix. In this sense, the topology of the system is protected by the the superconducting gap.

We can straightforwardly use this definition of topology in a disordered system to show the delocalization at the topological phase tran-

sition: when the invariant Q changes, $\det r$ has to change sign and becomes zero at the transition point. This means that $r^\dagger r$ has a zero eigenvalue and thus one perfectly transmitting channel opens through the wire.

1.4 Random-matrix theory

Multiple scattering by impurities or boundaries introduces an element of randomness in mesoscopic systems that calls for a statistical description. An ensemble of nominally identical systems, differing only in the configuration of impurities or the precise shape of a boundary, corresponds to an ensemble of random Hamiltonians or random scattering matrices. Random-matrix theory tries to make statistical predictions by choosing the ensemble of matrices as generic as possible, constrained only by fundamental symmetries. A variety of applications of random-matrix theory to mesoscopic transport problems are known, summarized in detail in the books and reviews available [14–17]. In the following we will focus on the aspects directly relevant to this thesis.

1.4.1 Symmetry classes

We have already encountered two fundamental symmetries: time-reversal and particle-hole symmetry. They both come in different forms, depending, for example, on the presence or absence of spin-rotation symmetry. In particular, both the time-reversal operator $\mathcal{T}$ and the particle-hole conversion operator $\mathcal{C}$ are anti-unitary operators that square to either unity or minus unity. The time-reversal symmetry in Eq. (1.4) is, for example, given by the operator $\mathcal{T} = \mathcal{K}\sigma_y$ ($\mathcal{T}^2 = -1$) and the particle-hole symmetry in Eq. (1.8) by $\mathcal{C} = \mathcal{K}\tau_x$ ($\mathcal{C}^2 = 1$), with $\mathcal{K}$ denoting complex conjugation.

Time-reversal and particle-hole symmetry can be written in the form

$$H = \mathcal{T} H \mathcal{T}^{-1}, \tag{1.12}$$

$$H = -\mathcal{C} H \mathcal{C}^{-1}, \tag{1.13}$$

using the time-reversal and particle-hole conversion operators. One generally classifies systems regarding the presence or absence of these symmetries and and whether their operators square to $+1$ or -1. This leads

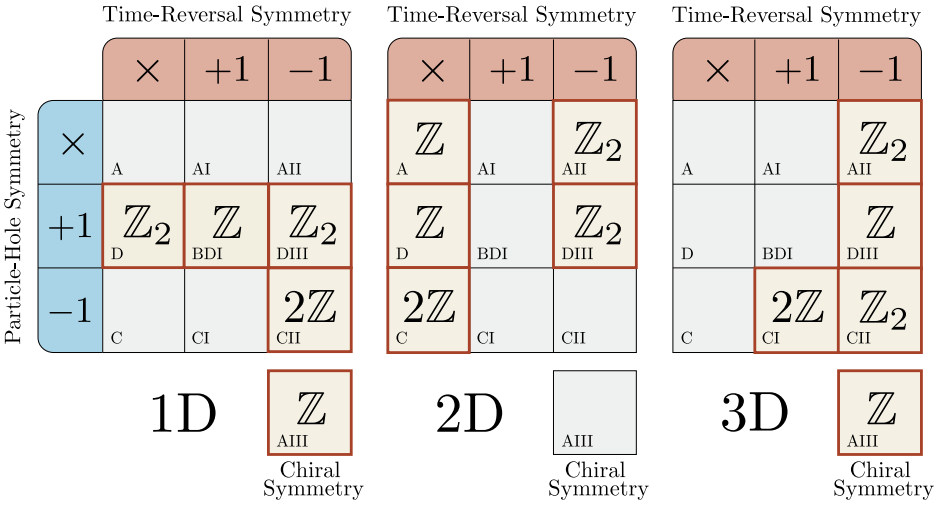

Figure 1.7. Classification of topological insulators and superconductors in one, two and three dimensions. For each dimension, the five symmetry classes in which topology is possible are indicated and the relevant types of invariants ($\mathbb{Z}$, $\mathbb{Z}_2$ or $2\mathbb{Z}$) are given. The symmetry classes are ordered depending on their time-reversal and particle-hole symmetry behavior: squaring to $+1$, -1 or absent ($\times$). The case of exclusive chiral symmetry is listed separately (symmetry class AIII). In the lower left corner of each box the name of the symmetry class is given. Design adapted from Ref. [18].

to nine different symmetry classes. A tenth symmetry class arises when we also consider the case where only chiral symmetry, $H = -\mathcal{T}\mathcal{C}H\mathcal{C}^{-1}\mathcal{T}^{-1}$, is present.

Each of these symmetry classes may or may not allow for topological invariants, depending on the dimensionality of the system [7]. An overview is given in Fig. 1.7, listing all the different symmetry classes and their formal names, which stem from Cartan's classification of symmetric spaces. The type of topological invariant if possible is given by the symbols $\mathbb{Z}$ (all integers), $\mathbb{Z}_2$ (0 or 1), and $2\mathbb{Z}$ (only even integers).

The examples of topological phases we discussed so far fit into this scheme as follows: in the quantum Hall effect (2D), no symmetries are present. Thus the relevant symmetry class is class A and topology is given by a $\mathbb{Z}$ topological winding number like in Sec.
refsec:WindingNumber. In the quantum spin Hall effect (2D) and the topological insulator (3D), time-reversal symmetry squares to -1 and

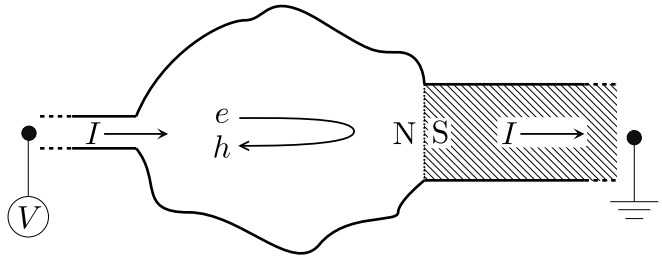

Figure 1.8. Chaotic scattering region with an interface between a normal metal (N) and a superconductor (S, shaded region). Andreev reflection at the NS interface converts a normal current (carried by electron and hole excitations e and h) into a supercurrent (carried by Cooper pairs). A normal metal electrode is connected to the dot via an N-mode point contact (narrow opening at the left). In this example the chaos is induced by the irregular shape of the dot region. Alternatively disorder in the scattering region does have a similar effect. The quantum transport phenomena in the setup can be characterized by a circular ensemble if the dwell time τ_D in the scattering region is much larger than the ergodic time $\tau_{\rm ergodic}$, the time scale on which a classical particle explores the whole phase space.

we are in class AII, with the $\mathbb{Z}_2$ topological invariants mentioned in Sec. refsec:othertopologicalphases. Finally, the Majorana wire (1D) of Sec. 1.3.1 obeys no time-reversal symmetry but a particle hole symmetry that squares to unity, placing it in symmetry class D with a Z_2 topological invariant.

1.4.2 Circular ensembles

The ensemble of scattering matrices used in random-matrix theory is called circular, because for a single scattering channel it would correspond to a uniform distribution of the phase shift on the unit circle. For N scattering channels the ensemble corresponds to a uniform distribution of the scattering matrix in the group of $N \times N$ unitary matrices, suitably restricted by the fundamental symmetries. Chaotic scattering by impurities or boundaries is known to be well described by a circular ensemble. An example relevant for this thesis is the chaotic normal-superconductor junction of Fig. 1.8. It is described by a unitary reflection matrix r and the electrical conductance is given by Eq. (1.10).

If no symmetry constraints are imposed on the unitary matrices, we call the ensemble of scattering matrices the circular unitary ensemble.

The presence or absence of time-reversal and/or particle-hole symmetry restricts the relevant matrix space to a smaller subset of unitary matrices, giving rise to several distinct circular ensembles.

1.5 Stroboscopic models

There is, up to now, still no rigorous analytical theory describing disorder-induced localization-delocalization transitions, including those that occur generically at a topological phase transition. Thus computer simulations are needed to calculate the scaling law and critical exponent associated with the diverging localization length at the transition.

Because the localization properties are universal, independent of microscopic details, we are free to choose a computationally efficient model even if it does not correspond to any particular physical realization. Stroboscopic models [19–22] are very well suited for this purpose since the propagation of wave functions is computationally very efficient for them, especially in higher dimensions. Although stroboscopic models do not correspond to a physical system in condensed matter, they can be realized experimentally with atomic matter waves in 1D optical lattices.

1.5.1 The quantum kicked rotator

A model is called stroboscopic when an otherwise freely propagating particle with kinetic energy $T(\boldsymbol{p})$ is subject to a driving potential $V(\boldsymbol{x})$ that is repeatedly turned on for an instant of time,

$$H = T(\boldsymbol{p}) + V(\boldsymbol{x}) \sum_n \delta(t - n\tau). \tag{1.14}$$

The period of the driving field is denoted τ. The prototypical example for a stroboscopic model is the so-called quantum kicked rotator [19–22], describing a particle with kinetic energy $T(p) = p^2/2m$ that is moving on a circle, $\theta \in [0, 2\pi)$, subject to the driving field $V(\theta) = K\cos(\theta)$. Consider such a particle, initially in a momentum eigenstate, $|\psi_0\rangle = \delta(p - p_0)$. The propagation of the wave function over one period of the driving field is given by a time evolution operator of the form

$$\mathcal{F} = e^{-iV(\theta)/\hbar} e^{-iT(p)/\hbar}, \qquad |\psi(t)\rangle = \mathcal{F}^t |\psi_0\rangle, \tag{1.15}$$

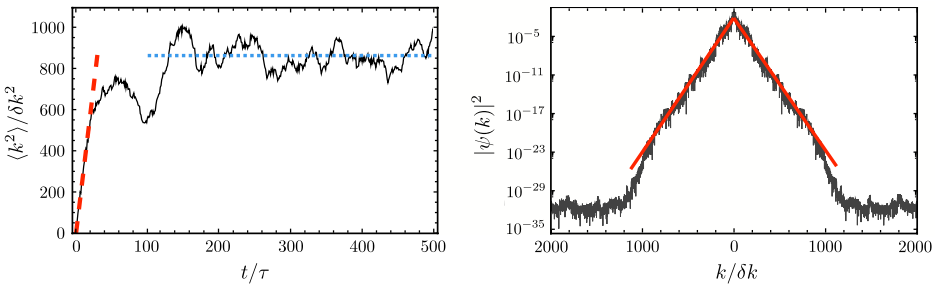

Figure 1.9. Particle in a quantum kicked rotator, initially in a momentum eigenstate $|\psi_0\rangle = \delta(p)$, is propagated in time. Left panel: Time dependence of the width of the wave function in momentum space. For a small number of kicks, the wave function spreads diffusively, $\langle k^2 \rangle \propto t$ (red dashed line). At larger times, interference effects become important and the wave function localizes, leading to a saturation of the spread (blue dotted line). Right panel: The wave function in momentum space after 1000 kicks. The exponentially localized shape is clearly visible (solid red lines, notice the logarithmic scale). Parameters used are $K = 6.66$ and $\hbar = m = 1$. Momentum is discrete with spacing δk due to the periodic real space.

also called Floquet operator. In the corresponding classical model, the particle performs a diffusive motion in momentum space over time, given a sufficiently large K. In the quantum kicked rotator, the particle wave function starts to spread diffusively in momentum space in the beginning but soon interference effects set in and the spreading slows down. For a large number of kicks, the spreading essentially stops and the wave function shows an exponentially localized shape, see Fig. 1.9.

1.5.2 Stroboscopic models in higher dimensions and the Anderson metal-insulator transition

Since the Floquet operator decomposes into two exponentials which are diagonal in real space and momentum space respectively, see Eq. (1.15), the computational cost of wave function propagation essentially reduces to two fast Fourier transforms. This is why stroboscopic models are computationally efficient. Another simplification arises for higher dimensional stroboscopic models since they can be simulated in one-dimension, as we will see in the following.

For example let us consider a three-dimensional stroboscopic model

of the form (1.14) with

$$T(\boldsymbol{p}) = \frac{p_1^2}{2} + \omega_2 p_2 + \omega_3 p_3, \tag{1.16}$$

$$V(\boldsymbol{x}) = K \cos x_1 (1 + \epsilon \cos x_2 \cos x_3), \tag{1.17}$$

and set $\tau = 1$ for brevity. If we choose the initial condition of a wave function as

$$\psi(x_1, x_2, x_3, t = 0) = \psi_1(x_1)\delta(x_2 - \phi_2)\delta(x_3 - \phi_3), \tag{1.18}$$

its propagation can be solved analytically in two of the dimensions:

$$\begin{aligned}\psi(x_1, x_2, x_3, t) &= \mathcal{F}^t \psi(x_1, x_2, x_3, t = 0) \\ &= \psi_1(x_1, t)\delta(x_2 - \phi_2 - \omega_2 t)\delta(x_3 - \phi_3 - \omega_3 t).\end{aligned} \tag{1.19}$$

Here, $\mathcal{F}$ is the Floquet operator of the model which decomposes into two exponentials just as in the example (1.15). The step to step evolution of the remaining dimension is given by a time-dependent Floquet operator

$$\psi_1(x_1, t + 1) = \tilde{\mathcal{F}}(t)\psi_1(x_1, t), \tag{1.20}$$

$$\tilde{\mathcal{F}}(t) = e^{-iV(x_1, \omega_2 t + \phi_2, \omega_3 t + \phi_3)/\hbar} e^{-ip_1^2/2\hbar}. \tag{1.21}$$

This is equivalent to the stepwise propagation of a wave function in a one-dimensional model with a time-dependent kicking potential of the form $V(x_1, \omega_2 t + \phi_2, \omega_3 t + \phi_3)$. The reduction from three to one dimension greatly simplifies the numerical simulation of the model. In the same way d-dimensional stroboscopic models can be reduced to a one-dimensional model, given that the kinetic term is linear in $d - 1$ dimensions.

The model considered here features an Anderson metal-insulator transition in momentum space. This means that when the parameter K is decreased (e.g. at fixed $\epsilon \sim 0.5$), the evolution of the wave functions changes: for large K they spread diffusively while for small K they localize (see phase diagram in Fig. 1.10). The corresponding one-dimensional model for this three-dimensional transition was realized experimentally with atomic matter waves in a cold atoms setup [23]. In the experiment, Cs atoms with kinetic energy $p_1^2/2$ were subjected to a stroboscopic kicking potential, produced by a pulsed standing laser wave. In this way the time evolution of $\psi_1(x_1)$ could be simulated, allowing for measurements

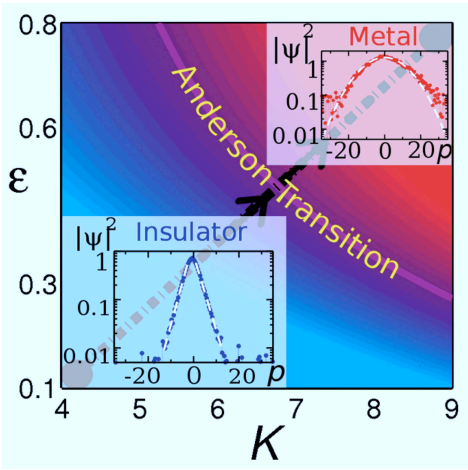

Figure 1.10. Phase diagram of the stroboscopic model in Eq. (1.17), from numerical simulations. The Anderson transition line separates the localized phase (blue) from the diffusive metallic phase (red). In the corresponding atomic matter wave experiment, the parameters were swept along the diagonal dash-dotted line. The insets show the experimentally observed momentum distributions, localized in the blue region and Gaussian in the diffusive (blue) region. From Ref. [23]. Copyright (2008) by the American Physical Society.

of the momentum distribution after some time of propagation. The critical exponent characterizing the divergence of the localization length at the transition could be extracted from these measurements and was found to be in accordance with numerical predictions.

1.6 This thesis

In the following a brief description of each chapter is given.

1.6.1 Chapter 2

When the chaotic superconducting scattering region introduced in Fig. 1.8 is coupled to two leads, also transport from one lead to the other becomes possible, see Fig. 1.11. The scattering matrix

$$S = \begin{pmatrix} r & t' \\ t & r' \end{pmatrix}, \tag{1.22}$$

for this situation is not solely a reflection matrix but also contains transmission blocks t and t'. Since the quasiparticles in a superconducting region are superpositions of electrons and holes they do not carry a definite charge and thus their transmission is not associated with an electrical current. But they have a fixed energy and carry a thermal current, with thermal conductance

$$G_{\text{th}} = G_0^{\text{th}} \operatorname{Tr} t^\dagger t = G_0^{\text{th}} \sum_n T_n, \tag{1.23}$$

at low temperatures T. Here, conductance is measured in units of $G_0^{\text{th}} = \pi^2 k_B^2 T/6h$ and we denoted the eigenvalues of $t^\dagger t$ by T_n.

In chapter two we study the thermal transport statistics of such a chaotic superconducting quantum dot using random-matrix theory. To this end we calculate the probability distribution $P(\{T_n\})$ of independent transmission eigenvalues from which all moments of the thermal conductance at the Fermi level can be extracted. We distinguish between four superconducting symmetry classes which give rise to four circular ensembles of scattering matrices, with distinct probability distributions. In this way we are able to deduce the generic influence of the symmetries on the thermal conductance, in form of weak (anti-)localization corrections. Compared to the statistics of the electrical conductance in non-superconducting ensembles, the most striking differences appear in the single-channel limit, which is not accessible in normal electronic gases. We show how this single-channel limit can be reached using a topological insulator or superconductor, without running into the problem of fermion doubling.

1.6.2 Chapter 3

In the third chapter we determine the influence of topology on the Andreev reflection properties of chaotic normal-metal–superconductor junctions. We already introduced the relevant setup in Fig. 1.8. The electrical conductance of the NS junction can be calculated from

$$G = G_0 \sum_n R_n, \tag{1.24}$$

following Eq. (1.10), but expressed in terms of the eigenvalues R_n of $r_{he}^\dagger r_{he}$, the so-called Andreev reflection eigenvalues.

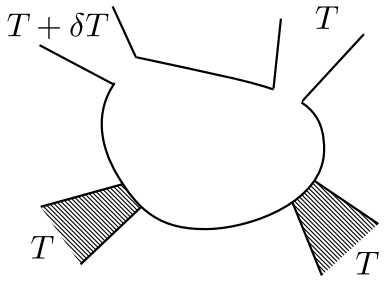

Figure 1.11. Quantum dot in a two-dimensional electron gas, connected to a pair of superconductors (shaded) and to two normal-metal reservoirs. One of the normal reservoirs is at a slightly elevated temperature $T + \delta T$. The second superconductor is needed to ensure the presence of time-reversal symmetry in the symmetry classes DIII and CI.

It is well established that the generic influence of symmetries on the conductance statistics can be determined by random-matrix theory. With the realization that topology constrains the reflection matrix just as symmetries do (e.g. $Q = \det r$ in symmetry class D), it becomes apparent that averaging over all possible reflection matrices of a symmetry class implies averaging over different topological phases. Since we want to disentangle the contributions from distinct topological phases we thus have to subdivide the known superconducting circular ensembles.

By calculating the probability distribution of the Andreev reflection eigenvalues R_n for these subdivisions of ensembles, we investigate the influence of topology on the electrical conductance G. We show that the dependence of G on the topological quantum number Q is non-perturbative in the number N of scattering channels. As a consequence a large-N effect such as weak localization cannot probe the topological quantum number. For small N we calculate the full distribution $P(G)$ of the conductance and find qualitative differences in the topologically trivial and nontrivial phases.

1.6.3 Chapter 4

The fourth chapter of the thesis introduces a setup for the unambiguous detection of topological superconductivity: a quantum point contact attached to a superconducting wire, as depicted in the inset of Fig. 1.12. The main part of the figure is a plot of the conductance G as a function of contact width or Fermi energy, showing plateaus at half-integer

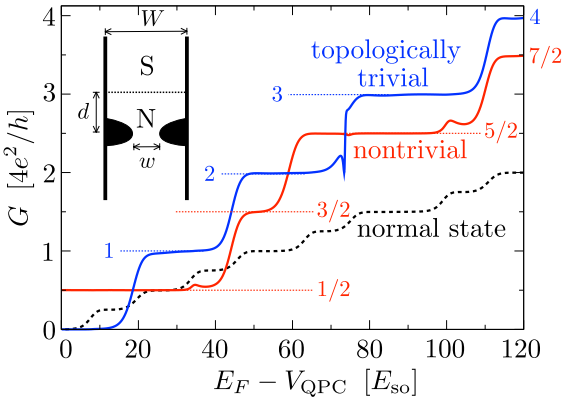

Figure 1.12. Conductance of a ballistic normal-metal–superconductor junction, with the superconductor in a topologically trivial (blue curve) or nontrivial phase (red curve). The black dashed curve is for an entirely normal system. By varying the potential V_{QPC} at constant Fermi energy E_F, the width of a point contact is varied in the setup (see inset).

multiples of $4e^2/h$ if the superconductor is in a topologically nontrivial phase. In contrast, the plateaus are at the usual integer multiples in the topologically trivial phase. Disorder destroys all plateaus except the first, which remains precisely quantized, consistent with previous results for a tunnel contact. The advantage of a ballistic contact over a tunnel contact as a probe of the topological phase is the strongly reduced sensitivity to finite voltage or temperature.

By now, experiments have demonstrated signatures of topology in superconducting wires, with one example summarized in Fig. 1.6. Nevertheless, the quantized nature of the conductance peak height has not been observed so far, presumably due to finite temperatures. The setup we propose here could be a step forward on the quest to detect this quantized peak height.

1.6.4 Chapter 5

In the fifth chapter the focus shifts to time-reversal invariant nodal superconductors. Although they are not topological in the usual sense, a variety of lower dimensional topological invariants can be defined that have strong impact on the transport properties of these systems.

Existing expressions for the topological invariant are based on the

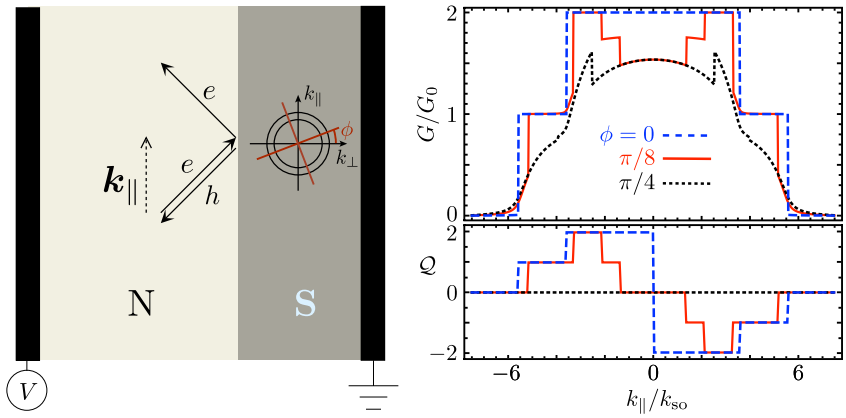

Figure 1.13. Left panel: reflection processes at a planar interface between a normal-metal and a gapless superconductor. The sketch in the superconducting region shows the Fermi surfaces and nodal lines for the specific case of a d-wave superconductor with Rashba spin-orbit coupling. Both the electrical conductance G and $\mathbb{Z}$ topological invariant $\mathcal{Q}$ are plotted for this case in the right panel, shown as a function of momentum $k_\parallel$ along the NS interface and angle ϕ between the interface and the nodal line of the superconductor.

Hamiltonian of an infinite system. We introduce an alternative formulation in terms of the Andreev reflection matrix of a planar normal-metal–superconductor interface (left panel of Fig. 1.13). This allows to relate the topological invariant to the angle-resolved Andreev conductance. We discuss a variety of symmetry classes that may arise depending on additional unitary symmetries of the reflection matrix. The condition for the quantization of the conductance is derived in each symmetry class and is tested on a model for a 2D or 3D superconductor with spin-singlet and spin-triplet pairing, mixed by Rashba spin-orbit interaction. The right panel of Fig. 1.13 shows our results for the case of a two-dimensional d-wave superconductor with spin-singlet pairing.

1.6.5 Chapter 6

In chapter six we introduce the concept of topology into stroboscopic models, explicitly constructing a two-dimensional periodically kicked system with a topological phase transition in the quantum Hall universality class.

Our model is essentially a stroboscopic version of the toy model in

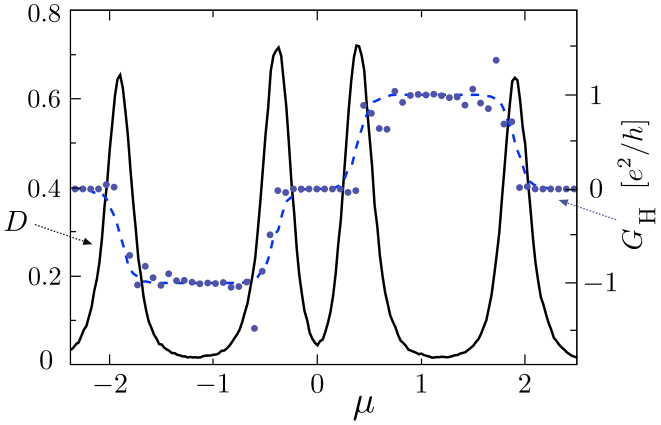

Figure 1.14. Left axis: Time-dependent diffusion coefficient (solid curve) after a sufficiently long time of propagation, showing four localization-delocalization transitions. Right axis: Four-terminal Hall conductance G_{H} (data points) and topological invariant $\mathcal{I}$ (dashed curve), demonstrating that these are *topological* phase transitions.

Sec. 1.2.1, combined with a localizing potential term. As we tune the system through a topological phase transition, the localization length of the system diverges. This can be observed in the time-dependent diffusion constant

$$D(t) = \langle \psi(t)|x^2|\psi(t)\rangle / t, \tag{1.25}$$

which converges to zero with increasing propagation time if the wave function localizes. In contrast it stays finite at the critical point. For our model D is plotted in Fig. 1.14 for a sufficiently large time, showing the presence of four localization-delocalization transitions where the topology of the system changes. We quantitatively investigate this localization-delocalization behavior, determining the critical exponent ν of the transition. Since the critical exponent is a universal property depending only on the symmetries and the dimensionality of the model, our result straightforwardly applies to corresponding solid state systems as well.

In order to obtain our results, we used the dimensional reduction scheme introduced in Sec. 1.5.2 and were thus able to study the quantum Hall transition in a one-dimensional system. Not only is this reduction to 1D computationally very efficient, it also provides a possible

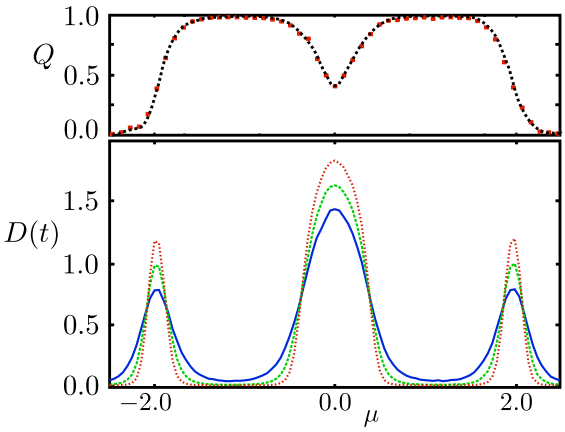

Figure 1.15. *Bottom panel:* Time-dependent diffusion coefficient for times $t = 10^6$ (red), $t = 10^5$ (green) and $t = 10^4$ (blue), showing three metallic regions. The points of intersection of these curves locate the metal-insulator transition. *Top panel:* Topological quantum number used to distinguish the topologically trivial ($Q = 0$) and nontrivial ($Q = 1$) insulators. In the metallic regions Q is not quantized.

route to perform experiments on the 2D quantum Hall effect using cold atoms in a 1D optical lattice. The approach we introduce in this chapter to investigate the quantum Hall transition can readily be generalized to other symmetry classes and dimensions, making it possible to study higher-dimensional systems in one spatial dimension as well.

1.6.6 Chapter 7

Following the methods introduced in chapter six we construct a stroboscopic model that realizes the $\mathbb{Z}_2$ topology of the quantum spin Hall effect. Due to the presence of time-reversal symmetry, the transition from the topological to the trivial phase does not happen directly as in the quantum Hall effect but only via an extended metallic region in parameter space.

This metallic phase is a bit unusual since wave functions spread faster than in a normal diffusion process. Thus the time-dependent diffusion coefficient does not tend to a constant value for large times, in contrast to the situation at the critical point. This is illustrated in Fig. 1.15 for our model. The plotted $\mathbb{Z}_2$ topological invariant was calculated

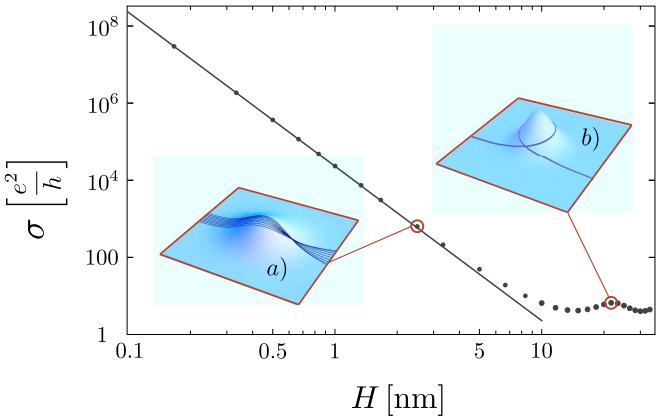

Figure 1.16. Surface conductivity of a topological insulator as a function of the height H of randomly positioned Gaussian surface deformations (width $W = 10\,\text{nm}$). The insets illustrate characteristic scattering situations that arise for different heights of the deformations. Dots represent numerical results whereas the line shows the analytical solution we derived in the shallow deformation limit.

using a scattering formulation that remains valid in the presence of disorder.

Once again we can use the dimensional reduction scheme to find an effective one-dimensional description of the localization behavior of the model. In the same way as in chapter six we study the delocalization at the metal insulator transitions quantitatively, finding that the critical exponent does not depend on the topological invariant, in agreement with earlier independent results from the network model of the quantum spin Hall effect.

1.6.7 Chapter 8

In chapter eight we consider the classical ballistic dynamics of massless electrons on the conducting surface of a three-dimensional topological insulator, influenced by random variations of the surface height. Since electrons traveling on the surface of a topological insulator are constrained to follow its geometry, they essentially move in a curved space. Their free motion is thus described by so-called geodesic lines, solutions of the geodesic equation of motion. In the presence of surface deformations these geodesic lines bend, a process we call geodesic scat-

tering. We solve the geodesic equation and the Boltzmann equation in the limit of shallow deformations to obtain the scattering cross section and the conductivity σ, see Fig. 1.16. At large surface electron densities n this geodesic scattering mechanism (with $\sigma \propto \sqrt{n}$) is more effective at limiting the surface conductivity than electrostatic potential scattering.

Bibliography

[1] M. Z. Hasan and C. L. Kane, Rev. Mod. Phys. **82**, 3045 (2010).

[2] X.-L. Qi and S.-C. Zhang, Rev. Mod. Phys. **83**, 1057 (2011).

[3] C. L. Kane and J. E. Moore, Physics World **24**, 32 (2011).

[4] C. W. J. Beenakker, arXiv:1112.1950, scheduled for vol. 4 of Annual Review of Condensed Matter Physics.

[5] J. Alicea, Rep. Prog. Phys. **75**, 076501 (2012).

[6] X.-L. Qi, Y.-S. Wu, and S.-C. Zhang, Phys. Rev. B **74**, 085308 (2006).

[7] S. Ryu, A. P. Schnyder, A. Furusaki, and A. W. W. Ludwig, New J. Phys. **12**, 065010 (2010).

[8] M. König, S. Wiedmann, C. Brüne, A. Roth, H. Buhmann, L. W. Molenkamp, X. L. Qi, and S. C. Zhang, Science **318**, 766 (2007).

[9] D. Hsieh, D. Qian, L. Wray, Y. Xia, Y. S. Hor, R. J. Cava, and M. Z. Hasan, Nature **452**, 970 (2008).

[10] Y. Xia, D. Qian, D. Hsieh, L. Wray, A. Pal, H. Lin, A. Bansil, D. Grauer, Y. S. Hor, R. J. Cava, and M. Z. Hasan, Nature Physics **5**, 398 (2009).

[11] P. A. Lee and T. V. Ramakrishnan, Rev. Mod. Phys. **57**, 287 (1985).

[12] F. Evers and A. D. Mirlin, Rev. Mod. Phys. **80**, 1355 (2008).

[13] V. Mourik, K. Zuo, S. M. Frolov, S. R. Plissard, E. P. A. M. Bakkers and L. P. Kouwenhoven, Science **336**, 1003 (2012).

[14] *The Oxford Handbook of Random Matrix Theory*, edited by G. Akemann, J. Baik, and P. Di Francesco (Oxford University Press, Oxford, 2011).

[15] P. J. Forrester, *Log-Gases and Random Matrices* (Princeton University Press, Princeton, 2010).

[16] M. L. Mehta, *Random Matrices* (Academic Press, New York, 1991).

[17] C. W. J. Beenakker, Rev. Mod. Phys. **69**, 731 (1997).

[18] T. Kitagawa, M. Rudner, E. Berg, and E. Demler, Phys. Rev. A **82**, 033429 (2010).

[19] G. Casati, B. V. Chirikov, F. M. Izraelev, and J. Ford, Lecture Notes in Physics, **93**, 334 (1979).

[20] F.M. Izrailev, Phys. Rep. **196**, 299 (1990).

[21] H.-J. Stöckmann, *Quantum Chaos: An Introduction* (Cambridge University Press, Cambridge, 1999).

[22] F. Haake, *Quantum Signatures of Chaos* (Springer, Berlin; New York, 3rd edition, 2010).

[23] J. Chabé, G. Lemarié, B. Grémaud, D. Delande, P. Szriftgiser, and J. Garreau, Phys. Rev. Lett. **101**, 255702 (2008).